

The Hubble Deep Field: Observations, Data Reduction, and Galaxy Photometry

Robert E. Williams, Brett Blacker, Mark Dickinson, W. Van Dyke Dixon¹, Henry C. Ferguson, Andrew S. Fruchter, Mauro Giavalisco², Ronald L. Gilliland, Inge Heyer, Rocio Katsanis, Zolt Levay, Ray A. Lucas, Douglas B. McElroy³, Larry Petro, Marc Postman
Space Telescope Science Institute, 3700 San Martin Drive
Baltimore, MD 21218

Hans-Martin Adorf, Richard N. Hook
Space Telescope European Coordinating Facility, c/o ESO, Karl-Schwarzschild-Str. 2,
D-85748 Garching, Germany

ABSTRACT

The Hubble Deep Field (HDF) is a Director's Discretionary program on HST in Cycle 5 to image an undistinguished field at high Galactic latitude in four passbands as deeply as reasonably possible. These images provide the most detailed view to date of distant field galaxies and are likely to be important for a wide range of studies in galaxy evolution and cosmology. In order to optimize observing in the time available, a field in the northern continuous viewing zone was selected and images were taken for ten consecutive days, or approximately 150 orbits. Shorter 1-2 orbit images were obtained of the fields immediately adjacent to the primary HDF in order to facilitate spectroscopic follow-up by ground-based telescopes. The observations were made from 18 to 30 December 1995, and both raw and reduced data have been put in the public domain as a community service. We present a summary of the criteria for selecting the field, the rationale behind the filter selection and observing times in each band, and the strategies for planning the observations to maximize the exposure time while avoiding earth-scattered light. Data reduction procedures are outlined, and images of the combined frames in each band are presented. Objects detected in these images are listed in a catalog with their basic photometric parameters.

¹Current address: Space Sciences Laboratory, University of California, Berkeley, CA 94720

²Hubble Fellow; Current address: Carnegie Observatories, 813 Santa Barbara Street
Pasadena, CA 91101

³Current address: Jet Propulsion Laboratory, California Institute of Technology,
4800 Oak Grove Dr., Pasadena, CA 91109

Subject headings:

1. Introduction

The HDF program is an outgrowth of previous, highly successful Hubble Space Telescope imaging projects which have elucidated the evolution of galaxies at high redshift. During Cycles 1 through 5, a variety of HST General Observer and Guaranteed Time Observer programs, as well as the Medium Deep Survey (MDS) key project, imaged distant galaxies in both cluster and field environments, providing (for the first time) kiloparsec-scale morphological data at all redshifts. The MDS used the WFPC-1 and WFPC-2 cameras in parallel mode to image random galaxies near the fields of targeted objects. Analyzing 144 field galaxies having $I < 22$ from six fields, Driver, Windhorst, & Griffiths (1995) found from visual classification that early-type spirals, ellipticals, and late-type spirals/irregulars were observed in roughly equal proportions, with the Sd/Irr's having much higher surface density than their counterparts at the current epoch. Driver et al. (1995) extended this analysis with a similar study of one very deep field for which they showed that galaxy counts beyond $I = 22$ continue to be increasingly dominated by Sd/Irr galaxies. Combining ground-based redshift information with HST imaging, Lilly and collaborators obtained B and I images for 32 galaxies from their CFHT survey ($17.5 < I < 22.5$) with known redshifts in the range $0.5 < z < 1.2$ (Schade et al. 1995). They found that the observed galaxy morphologies were similar to those seen locally, but that the B images (rest frame UV) looked far less regular than observed at longer wavelengths. In addition, they determined that the central surface brightnesses of the disks in their sample of late-type spirals were more than 1.2 magnitude brighter than found locally. Also, they found that many of the bluer galaxies were nucleated, and they concluded that both of these effects must be responsible for much of the observed evolution of the luminosity function of blue galaxies.

Other HST programs targeted galaxies with known redshifts based upon their membership in clusters that had been studied from the ground, e.g., 0939+4713 (Dressler et al. 1994a,b) and the cluster(s) associated with the radio galaxy 3C 324 at $z = 1.21$ (Dickinson 1995a). Both of these programs demonstrated the ability of the refurbished HST to resolve galaxy structure at moderate to high redshift in a way that made morphological classification and a quantitative study of various parameters possible. Cluster 0939+4713 does not look entirely unlike nearby clusters insofar as it is populated largely by spiral and elliptical galaxies. However the disk systems are bluer and more numerous than spiral galaxies in the cores of clusters today, and often show signs of disturbance and tidal

interactions. Evidently, these spirals are responsible for the rapidly evolving blue galaxy population first noted in distant clusters by Butcher & Oemler (1978; 1984). Looking back to $z = 1.21$, the cluster associated with 3C 324 includes apparently normal, mature E/S0s, but readily recognizable spiral galaxies appear to be rare, and a large number of irregular, amorphous objects are present (Dickinson 1995a,b). Since the first servicing mission, HST has imaged a number of other distant galaxies at still higher redshifts of $1 < z < 3.5$ (c.f. Cowie, Hu, & Songaila 1995; Giavalisco, Steidel, & Macchetto 1996)

While much of the information available in these images remains to be interpreted, two things have become clear. First, HST can indeed resolve galaxy-sized systems out to high redshift. Second, the Universe at high redshift looks rather different than it does at the current epoch. The fact that HST can image galaxies back at epochs when they were apparently forming and evolving rapidly is of fundamental importance to our understanding of galaxy evolution, and it is imperative that this capability be fully exploited. Based on the current excellent performance of the telescope, a decision was made to devote a substantial fraction of the Director's Discretionary time in Cycle 5 to the study of distant galaxies. A special Institute Advisory Committee was convened which recommended to the Director that deep imaging of one 'typical' field at high galactic latitude be done with the Wide-Field Planetary Camera 2 (WFPC-2) in several filters, and that the data be made available immediately to the astronomical community for study. Following this recommendation a working group was formed to develop and carry out the project.

It is not our purpose here to interpret the data, but rather to present the images and source catalogs, along with the necessary background to facilitate the use of the HDF in studies of galaxy evolution. As part of the background, we describe the criteria for selecting the field, the scientific rationale for the selection of filters, technical aspects of planning the observations, and details of data reduction and calibration. The images are presented and discussed in §5, and the source catalogs in §6. In view of the wide interest in these observations, we have tried to provide a useful reference work, being reasonably comprehensive in describing the data reduction, and including in printed form the most important photometric parameters for the detected sources. Nevertheless many of the parameters for the individual galaxies (e.g. S/N in the different bands, higher-order image moments, star/galaxy classifications) have been left out of the printed catalog. We have opted to emphasize black & white over color images to provide as much detail as possible in the limited dynamic range of the printed page. The full catalog and color images are maintained on the STScI world-wide web site at <http://www.stsci.edu>.

2. Field Selection

2.1. Primary Field

One of the suggestions to the Advisory Committee by the Institute was that a field in one of the continuous viewing zones (CVZ) be considered, because the observing efficiency there could be up to a factor of two higher than other locations on the sky. The working group focused its attention on the northern CVZ, thereby constraining the HDF location to a narrow declination range centered around $+62^\circ$. In addition to being in the CVZ, the candidate field would have to have low optical extinction ($E(B - V) < 0.01$ mag), low HI column density ($< 2.5 \times 10^{20}$ cm $^{-2}$), and low FIR ($\lambda = 100\mu\text{m}$) cirrus emission. Furthermore, to facilitate faint object studies at many wavelengths, the HDF field would need to avoid known bright sources in the x-ray, UV, optical, IR, and radio passbands. This latter criterion, therefore, excluded areas with known nearby ($z < 0.3$) galaxy clusters. Visual inspection of IPAC's co-added $100\mu\text{m}$ IRAS maps was used to select regions with no significant Galactic cirrus features. An initial sample of about 20 possible HDF regions was narrowed to 3 optimal candidates, all within the Ursa Major region. Quick VLA snapshots at 3.6 and 21 cm by Kellermann (1995) reduced the choice to two fields due to the presence of a 68 mJy source in the center of one of the fields. Initial optical selection was based on the digitized Palomar sky survey. Eisenhardt (1995) kindly provided KPNO 4m R-band CCD images (2×300 second exposures) as further verification that the fields were typical in terms of source counts, and were not affected by scattered light or diffraction spikes from bright stars outside the field

A search of the ROSAT data archive (Petre 1995) in the vicinity of the two remaining field candidates placed a conservative upper limit on the flux from any source of 6×10^{-14} erg cm $^{-2}$ sec $^{-1}$ in the 0.1-2.4 keV band.

In June 1995, HST acquired a single orbit F606W observation of each of the two fields to verify guide star acquisition. In order to be conservative in safeguarding the entire sequence of HDF observations, we required an independent pair of back-up guide stars, which are scarce at this high Galactic latitude. The decision between the two remaining candidate fields was thus based on guide star availability. The location and characteristics of the resulting HDF field are given in Table 1, and the KPNO R-band image of the field telescope is shown in Fig. 1 with the WFPC-2 field of view superposed.

2.2. Flanking Fields

During the HDF observations, 10 orbits were devoted to short exposures of eight “flanking” fields adjacent to the main survey region. These fields were arranged in a roughly square pattern surrounding the central HDF, as shown in Fig. 1. All exposures in the flanking fields were taken at the same orientation as the central field. The coordinates for these fields are given in Table 2.

3. Filter Selection

The selection of filters for the HDF observations represents a balance between the desire for depth and the desire for color information and practical considerations involving scattered earth light.

The HDF observations were not aimed at answering one specific question, but are rather intended to be of general use for constraining models of galaxy evolution and cosmology. There was thus no single, well-defined criterion that could be used to develop the optimum observing strategy. For galaxies that are well resolved, color gradients and the dependence of morphology on wavelength are of interest. If such studies were the sole aim of the observations, the best strategy might be to opt for the highest possible S/N in two widely separated bandpasses. On the other hand, for the more numerous faint and barely resolved galaxies, it is the statistical distributions of color vs. magnitude, color vs. angular size, etc. that are of interest. These provide information on both the redshift distribution and the stellar populations of the galaxies. For galaxies fainter than spectroscopic limits, it is important to have at least two colors. A single color (or “spectral index”) is less useful because there is no way to separate effects of the intrinsic rest-frame spectral properties from the effect of the k -correction. This argues for observations through at least three filters, preferably with the highest possible efficiency and with minimal overlap in bandpasses. While other options offer slightly better photometric accuracy or slightly less bandpass overlap, the combination of F450W, F606W, and F814W provides a very efficient way to cover the optical portion of the WFPC-2 bandpass (Fig. 2). The addition of observations through the F300W filter greatly improves the leverage for statistical redshifts. These observations cannot reach the limiting depth of the other three filters because of the low detector quantum efficiency (QE) at 3000 Å. However, because of the low QE, the F300W data are largely read-noise limited, whereas the other bands are more nearly sky-noise limited. Thus the the F300W observations can make use of the orbital “bright time” (see below) that is not particularly useful for the other filters.

With this four-filter strategy the HDF reaches depths roughly three magnitudes fainter than the deepest ground based images in the red bands, two magnitudes deeper in the B band, and one magnitude deeper in the U band. The 80% completeness limit of current deep spectroscopic surveys is $B_{AB} \sim 24$ ⁴ and $I_{AB} \sim 22.5$ (Glazebrook et al. 1995; Lilly et al. 1995). With Keck and other large aperture telescopes, these limits may be pushed one or even two magnitudes fainter. Even then, the faintest two or three magnitudes of the HDF survey are beyond current spectroscopic limits. Hence, for at least the next few years, the primary information on the redshift distribution of these very faint galaxies will come from statistical analysis of the color distribution. In the individual F450W, F606W, and F814W bands, the HDF observing strategy provides only a modest improvement over the deepest existing HST images. However, having four passbands provides essential information not available from previous surveys.

Part of the scientific interest in F300W stems from its utility in searches for very high-redshift ($z > 3$) galaxies (Guhathakurta, Tyson, & Majewski 1990; Steidel & Hamilton 1992,1993) The intrinsic 912Å Lyman break in galaxies, combined with the increasing opacity of the intergalactic medium at high redshifts produces a distinctive feature in the spectra of high-redshift galaxies (Yoshii & Peterson 1994; Madau 1995). Specific color selection criteria for the HDF bandpasses are described by Madau et al. (1996). The F300W filter has a small but significant “redleak” at 8000Å. The transmission curve of this redleak is similar to that of the F814W filter, but the throughput is three orders of magnitude smaller. Thus, a 20th magnitude galaxy with no intrinsic flux in the F300W bandpass will appear as an F300W source of AB magnitude ~ 27.7 . Most of the galaxies detected in the HDF have magnitudes fainter than $I_{814} = 23$, and would thus be below the detection limits of the F300W images unless they have intrinsic emission near 3000Å.

3.1. Scattered Light and Observation Scheduling

The choice of the F300W passband was motivated partly by the desire to provide a measure of the surface density of galaxies above redshift $z = 3$ and partly by the desire to find an observing strategy that avoids contamination from stray earth light. While the zodiacal-light background in the HDF field is extremely low in December, scattered earth light during portions of the CVZ was expected to dominate the background in F450W, F606W, and F814W. The scattered earthshine in the F300W filter is more than 15 times fainter than in the other three filters due to absorption of the solar flux by ozone in that

⁴Most magnitudes in this paper are expressed in the *AB* system (Oke 1974), where $m = -2.5 \log f_\nu - 48.60$.

band. HST can in principle observe to within 15.5 degrees of the bright earth limb and 7.6 degrees of the dark limb (these limits are imposed by the Fine Guidance Sensors). However, the effects of scattered light can be detected in archival WFPC-2 images at angles to the bright limb as great as 40 degrees. The amount of scattered light in the HST focal plane varies both with limb angle and the total brightness of the earth. The observations were carefully scheduled to make use of the dark portion of the orbit for observations through the F450W, F606W, and F814W filters, and the bright portion for F300W observations.

Efforts over the last two years to understand the sources of background have resulted in the development of a program (SEAM; Bely et al. 1996) that successfully models the WFPC-2 background as a function of wavelength and viewing direction. SEAM has been used to predict the background in various filters considered for the HDF. Figure 3 shows examples of the predicted background as a function of time in several orbits spaced throughout the program. Curves such as these were used to plan the start and stop times of each observation to maximize observing time, while minimizing the total background. To ensure that the timing was correct, the start/stop times were adjusted using the latest available orbit predictions as a last step before the final schedule was frozen several weeks prior to the observations.

It should be emphasized that without this careful scheduling of the observations, the extra observing time gained by selecting a field in the CVZ would have been largely wasted. While such micro scheduling is not something that is routinely done for HST observations, it is clearly something that is desirable to implement in a more automated manner for observations in which sky background is the limiting factor in obtaining the best signal-to-noise ratio.

Another decision made in the planning stage was to attempt to obtain observations at nine separate pointing positions through each filter. The $0.1''$ pixels of the three wide-field (WF) cameras in the WFPC-2 instrument undersample the point spread function of the telescope, while the planetary camera (PC) provides more nearly optimal sampling. The motions of the telescope were laid out as non-integer multiples of a WF pixel. This “dithering” reduces the photometric errors due to flatfielding uncertainties and also allows reconstruction of a higher-resolution image because sources are sampled in different portions of a pixel at each dither position. The price for these improvements is increased complexity in the data reduction phase. The images must be aligned and resampled to the same pixel scale, correcting for the geometric distortions introduced by the camera optics. We chose to observe at nine dither positions spanning a range of 2.6 arcseconds that would in addition map to nine independent positions within the (WF) pixel scale of 0.1 arcseconds (Fig. 4). Two unplanned dither positions with offsets of $\sim 1''$ and a rotation of 4.3 arcminutes

resulted from an 11 hour period in which one of the Fine Guidance Sensors locked up on a secondary extremum of the “S-curve.” We tried to obtain at least five exposures per filter per dither position that were near enough in time that slow drifts in the telescope pointing (which had been seen in previous CVZ observations) would not complicate the cosmic-ray rejection process.

4. Data Reduction

4.1. Pipeline

The HDF data were reduced three times. Version 1 reflects processing up to January 15, 1996. Version 2 was released February 29, 1996 and is used for this paper. At the time of writing, version 3 was still a month or two from completion.

The HDF data were reduced using the same software as the standard HST pipeline calibration, the STSDAS task `calwp2`, but with different calibration files and a slightly modified treatment of the darktime. The calibration procedure is fully documented in the HST Data Handbook (Leitherer 1995). For the HDF, several of the calibration files were improved by combining a number of individual calibration frames to produce “super” calibration frames. We discuss these improved calibration files below. Versions 1 and 2 used the same calibration files. These are being modified for version 3, for reasons that will be outlined below.

The superbias frame. To the charge accumulated in each pixel of the WFPC-2 CCDs is added a bias value, designed to keep the output of the analog-to-digital (A/D) conversion consistently above zero. The value of this bias can vary slightly with position across the chip. A bias reference file is therefore subtracted from the data to remove any position-dependent bias pattern. The HDF used a superbias frame constructed from 160 individual bias frames. These frames, in uncalibrated format, were retrieved from the archive in sets of 40 and calibrated (A/D conversion and overscan subtraction) in the standard way. Each set of frames was then combined into a single image with cosmic rays removed. The resulting 40-frame bias images were used to create superdark images (see below) for each epoch. Because of the timing in the WFPC-2 electronics, bias frames are not really zero-length exposures, but have 43.6 seconds (plus the readout time for each chip) of exposure time. To remove this, the superdarks were normalized to exposure times of 43.6 s and subtracted from the superbias. The dark-subtracted bias frames were then averaged to produce the final superbias frame. To use the file correctly, the DARKTIME

header field in the frame to be calibrated is updated to the value

$$DARKTIME = 60 \times \text{int}((t + 16.4)/60.) + 43.6, \quad (1)$$

where t is the integration time of the image in seconds. The standard calwp2 data reduction software will then scale the superdark appropriately, and the dark current remaining in the bias frame will be removed in the superbias subtraction. The version 3 data reduction will use bias frames taken both before and after the observations so any systematic drifts with time will be better averaged out.

The superdark and delta-superdark frames. The dark subtraction is intended to remove spatial structure present in the thermally-induced dark current. In practice, most of this structure is in the form of individual “warm” pixels that are between 2σ and 5σ deviant from the mean, but are relatively stable over long periods of time. The superdark frame used in the HDF is derived from eight sets of 30 individual calibrated dark frames (1800 second exposures taken with the shutter closed). The frames in each set were combined and cosmic rays removed, then the eight sets were combined into a single file. The resulting image was normalized to a darktime of 1.0 second.

A significant fraction of the counts seen in WFPC-2 “dark” frames arise from cosmic-ray glow in the MgF_2 faceplates in front of the CCD’s. This glow varies with the cosmic ray rate and for version 3 will be subtracted independently of the thermal dark current in the CCD detector. For versions 1 and 2, variations in the amplitude of the MgF_2 glow were ignored (i.e. the superdark was scaled by exposure time and no correction was made for the cosmic ray rate). The result is that individual images, after flatfielding, typically show curvature in the background of a few percent within 200 pixels of the edge of the chip. These variations in background average out to less than 1% when multiple frames are stacked together.

To flag the hot pixels present at the start of the HDF observations, a delta-superdark frame was created. To do this, 11 dark frames (total exposure time 19000 seconds) taken near the start of the HDF observations were averaged together. The superdark frame was subtracted and pixels more than 5σ deviant from the mean were identified. (Note that “cold” pixels — i.e. those less than -5σ deviant — were also identified.) These pixels were added to the superdark frame (so that they would subtract, to first order, from the individual observations), and were also flagged in the data quality file, ensuring that they would be ultimately rejected in the final combinations of the images at the different dither positions. The delta-superdark was the same for versions 1 and 2, but is being remade for version 3.

The flat-field frames. The flat-field frames developed for the HDF have since become the default flats for the HST pipeline calibration. These files are versions of the original

Investigation Definition Team (IDT) flats with an improved on-orbit illumination correction applied to scales greater than seven pixels. On the very largest scales, the chip-to-chip normalization of the IDT flats have been preserved. Tests of independent sets of flat-field images suggest that the uncertainties are less 2 %. More information on these files can be found in the WFPC-2 Cycle 4 Calibration Summary (Baggett, Casertano, & Biretta 1995). For version 3 of the HDF data reduction, more recent versions of the flat-field calibration files are being used.

4.2. Cosmic Ray Rejection and Initial Image Stacking

The preceding steps in the data reduction were identical for versions 1 and 2 of the HDF data. The versions diverge at the image combination step in two ways: (1) the individual images were weighted differently in the two versions and (2) care was taken in version 2 to remove satellite and space-debris trails from the images.

Cosmic ray (CR) identification was carried out using the *stsdas* task *xcrrrej* (a modified version of the standard *STSDAS crrej* task). This program is a more sophisticated implementation of the simple idea of averaging several images of a target while removing cosmic ray events. The process begins by computing sky levels from the histogram of pixel intensities, estimating the best value by parabolic interpolation of the peak and the two adjacent points in the histogram. These sky levels are subtracted and the images are renormalized to the average exposure time to allow CR rejection on frames with differing backgrounds and exposure times. The program then computes the expected RMS deviation in each pixel based on the minimum observed value in that pixel and a model for the noise that includes Poisson noise, read noise, and a noise proportional to the counts (to account for variations in the peak brightness of bright sources, e.g. due to pointing jitter). In the first pass values more than 6σ above minimum are rejected. In the second pass, the average in each pixel is used as the expectation value, and values more than 5σ above and below the average are rejected. In the third pass the average is again used and values more than 4σ above and below are rejected.

Typical cosmic rays seen in WFPC-2 are not single-pixel events. To remove the wings of cosmic rays, pixels adjacent to rejected pixels are rejected if they are deviant by one-half the sigma-threshold applied to the initial rejected pixel.

In version 1 of the HDF processed data, the images were combined with weights proportional to exposure time. This is nearly optimal for F606W, and F814W, but not for the F450W and F300W images, which have a significant read-noise contribution. For

version 2, the images were combined with weights proportional to the inverse-variance at the mean background level. The variance, in electrons, at the sky level is computed from the noise model:

$$\sigma^2 = bt + dt + r^2 \quad (2)$$

where t is the exposure time, b is the sky background rate, d is the dark current, and r is the read noise. Pixels affected by cosmic rays were not used in the combination and were set to zero in the output inverse-variance image. These output inverse-variance images were used to compute the weights for the final combined images as described in §4.6 below.

4.3. Hot Pixel Removal

The number of hot pixels is minimized by using the delta-superdark frame in the HDF pipeline; however, several thousand remain in each frame after pipeline processing.

“Growing pixels” are hot pixels that have appeared or disappeared since the delta-superdark. They were identified by combining sets of images taken at different dither positions, subtracting a 5×5 pixel median filtered image to remove residual objects, and identifying pixels that deviate from 0 by more than 5σ . A growing-pixel mask was created for each day using about 48 hours of data roughly centered at noon UT. The masks for each day were logically OR’ed together and OR’ed with the static mask (the list of constant WFPC-2 bad pixels) and the delta-superdark data quality file (the list of pixels that became hot between the superdark and the delta-superdark). In other words, a pixel flagged as suspect in any one of these files was marked in the final data quality file, and ultimately rejected in the final image combination.

This procedure reduces the number of hot pixels to about a dozen per chip. These are identified with a program that flags individual pixels more than 6σ deviant from their neighbors in a 3×3 box. These pixels are OR’ed into the mask to produce one final mask that flags all pixels that were suspect at any time during the HDF. Altogether roughly 12000 pixels per chip were masked. Because there are eight or nine dither positions per filter, this conservative approach to masking hot pixels has only a modest effect on the final signal-to-noise ratio, reducing it by about 10% in the pixels that were flagged, and this for only about 2% of the total imaging pixels.

4.4. Scattered Light Removal

The HDF observations were carefully scheduled to minimize the effect of scattered light. Nevertheless, scattered light from the bright earth produces a visible X pattern in about 25% of the HDF data frames. The X pattern is caused by shadowing of the scattered light by the mirror supports in the WFPC-2 relay optics (Biretta, Ritchie, & Rudloff 1995). Images with a mean background more than a few times higher than the mean for a given bandpass were excluded from the processing. However, most of the affected frames had only a small amount of scattered light, and the S/N was not significantly degraded. These images were used in version 2, and steps were taken to remove the scattered light before combining them with the unaffected frames. Briefly, the scattered light subtraction was done by registering the bright and dark images, subtracting the dark from the bright to remove the sources, smoothing to remove any residual sources left over after subtraction, and subtracting this smoothed “sky” image from the bright frame. This procedure removed the X pattern to within a few percent.

4.5. Image Registration and Geometric Distortion Correction

The HDF observations were carried out with nine to eleven different pointing positions per filter, spanning a range of roughly 2.6 arcseconds (Fig 4). After having been fed through the pipeline, the registration of the individual images was checked by comparing the positions of several bright sources. This revealed two unexpected large (0.98 arcsec) shifts, but otherwise suggested that the images at each dither position were registered to within the errors of such a comparison. The images with the large shifts have been treated as separate dither positions.

The roughly five images per dither position were cosmic-ray rejected and stacked into a single image. In order to measure the shifts and rotations between these stacks, these images were first geometrically undistorted and resampled using the “drizzle” task which is described below. The drizzle program, in turn, removes geometric distortion using the polynomial solution described by Trauger et al. (1995). The shifts and rotations between the dither stacks were then measured using a cross-correlation-based technique on each of the three wide-field chips and averaging the results, again using the relative orientations and positions of the chips measured by Trauger et al. (1995).

Except for the two unexpected dither settings with a rotation of 4.3 arcmin, all other exposures align perfectly to an accuracy of less than 0.1 arcmin rotation, the estimated measurement error. Estimated errors in the shifts are a few hundredths of a pixel for

F450W, F606W, and F814W. At the time of this writing, the shifts and rotations have not been checked to the ultimate possible precision in each of the input frames. There is thus some possibility of improving the resolution and shape of the final PSF with a more careful combination of the images. However, we anticipate such processing will produce only a few percent gain in S/N at the faintest levels, and a modest additional gain in the ability to distinguish stars from galaxies.

Once the shifts and rotations were measured, the images were aligned and combined using the “drizzle” algorithm, which corrects for geometric distortion and produces an output image that is sampled on a smaller pixel scale than the input images. The final pixel scale chosen for both the PC and WF chips was 0.4 of the original WF pixel or, using the astrometric solution of Trauger et al. (1995) for WF2, 0.03985 arcsec.

4.6. Image Combination

The “drizzle” algorithm was developed for the combination of multiple stacks of dithered, geometrically distorted, undersampled image frames. It was used to produce the combined output images of the HDF project from the flat-fielded, cosmic ray and hot pixel cleaned stacked frames corresponding to the different dither positions. The algorithm, which is more formally known as variable-pixel linear reconstruction, will be described in detail in another article (Fruchter & Hook 1996). Here an overview is provided for those interested in understanding the specific processing of the HDF.

The algorithm is conceptually simple. Pixels in the original “input” images are mapped into pixels in the subsampled “output” images, taking into account shifts and rotations between images and the optical distortion of the camera. The final image is built up by averaging together enough images taken at different positions that non-uniformities in exposure time from pixel to pixel in the output image become inconsequential (and are in any case recorded in the output variance map).

If there are enough input images, a simple way to improve the resolution of the output image is to make the area or “footprint” of each pixel in the input frame smaller than the physical pixel size, before mapping it onto the output image. To carry forward the analogy, these shrunken pixels, or “drops”, rain down upon the subsampled output image. In the case of the HDF, the drops had linear dimensions one-half that of the input pixel — slightly larger than the dimensions of the output subsampled pixels. The flux in each drop is divided up among the overlapping output pixels in proportion to their areas of overlap. In the code this is done by breaking the drops into $N \times N$ “droplets” and distributing their

flux among the output pixels. The version 1 and version 2 images were made with $N = 12$. For version 3, the code has been revised to calculate the overlap exactly.

The position of each droplet in the undistorted, subsampled output image is computed and its value is averaged with the previous estimate of that pixel value. This is a weighted average which uses the assigned weight for the droplet and a weight for the previous estimate which is the sum of the weights of all droplets previously averaged into the output pixel. The image value and weight of the output pixel are updated before considering the next droplet. Thus, if a particular drop with value i_{xy} and weight w_{xy} is to be added to an image with value I_{xy} and weight W_{xy} , the resulting value of the image I'_{xy} and weight W'_{xy} is

$$I'_{xy} = \frac{i_{xy}w_{xy} + I_{xy}W_{xy}}{w_{xy} + W_{xy}} \quad (3)$$

$$W'_{xy} = w_{xy} + W_{xy} \quad (4)$$

This procedure is performed for each of the N^2 droplets in each of the pixels of the input image. In order to preserve resolution, a drop size is used which is smaller than the input pixel size. A particular output pixel may receive no droplets when drizzling an individual input frame. In Figure 6 the top left output pixel represents such a situation. These “zero valleys” are not a concern as long as there are enough input frames with different sub-pixel dither positions to fill in the image. It is, in the end, the placement of the dither positions which determines how small the drop size can be.

This scheme was developed in part as a quick means of implementing an area-weighted interpolation for distorted pixels, similar to the interpolation scheme proposed by Trauger et al. (1995). The weight of a droplet from a particular pixel is just $1/N^2$ times the weight of the pixel, which was computed as described in §4.2. Therefore, to the extent that N is large, the weight of a particular input pixel in a final output pixel is the fraction of the input pixel overlapping with the output pixel times the input pixel weight.

This algorithm has the following characteristics. (1) It preserves both surface and absolute photometry; flux density can be measured using an aperture whose size is independent of position on the chip. (2) It handles missing data due to cosmic ray hits and hot pixels. (3) It uses a linear weighting scheme which is statistically optimum when inverse variance maps are used as weights. These weights may vary spatially to accommodate changing signal-to-noise ratios across input frames (e.g. due to variable scattered light). This spatial variation was not included for versions 1 and 2 of the data reduction. (4) It produces an inverse variance map (the weight map) along with the combined output frame. (5) It preserves resolution. (6) It largely eliminates the distortion of absolute photometry

produced by the flat-fielding of the geometrically distorted images. In an uncorrected image the total photometry of sources near the corners of the chip is about 3.5% brighter than an equivalent source at the center of the chip (Biretta 1995).

Drizzling does however produce small artifacts in the final image. The interpolation scheme used produces an output image that is optimal for aperture photometry when the output image is weighted by the inverse variance. However, it is not optimal if one is interested primarily in producing a smooth point spread function (PSF). Simulations of the dithering pattern and drizzle parameters used in the HDF show that even in the absence of Poisson errors, drizzling produces a PSF whose FWHM varies by $\pm 5\%$ and whose shape can show noticeable high-frequency “noise”. Both of these effects depend upon the pixel phase of the star relative to the dither positions, and thus are hard to predict for any individual object. (This directly limits the possibility of applying deconvolution, a process that amplifies high frequencies, to the drizzled data.) In Fig. 7 we show an example of a PSF from a star in the HDF. Variation about a Gaussian fit is a natural feature of an image convolved with large square pixels. However, because the shifts between images in the HDF do not uniformly sample the plane, the interpolation scheme used in drizzling makes this high-frequency scatter even more apparent.

The observed variations could have been reduced by using a larger final pixel size. However, doing so would have meant either using a different pixel scale for the PC than for the WF or suffering even further degradation of the PC resolution. While the high frequency scatter will affect attempts to fit the PSF, it does not significantly affect aperture photometry. By a radius of two WF pixels (five pixels in the drizzled HDF images), which is an aperture frequently favored by those doing HST photometry in crowded regions, the scatter is essentially gone. Furthermore, the scatter is seen only where the variations in surface brightness of an object are so rapid that they are undersampled in the original image (point sources, for example). Those for whom the scatter is a problem may wish to convolve the image with a narrow Gaussian, and thus trade a little resolution for a smoother PSF.

Drizzling also causes the noise in one pixel to be correlated with the noise in an adjacent one, because a single pixel from an input image typically affects the value in several output pixels, even though most of the power often goes into a single output pixel. The amplitude of this effect is determined by the footprint, or drop size, of the input pixels and by the positions of the sub-pixel dither points. If the data had been combined using the shift-and-add technique, which has a pixel footprint four times larger than that used in the HDF, this effect would have been substantially greater.

The drizzling parameters used in the HDF produce negligible correlations between pixels which are not adjacent. The measured 3×3 correlation matrix of adjacent pixels

in the F606W frames is shown in Table 3. It includes any correlation in the sky due to inexact flat fielding or true variations in the sky. In the end, this provides a better idea of how sky noise will be reduced as the size of an aperture is increased. The correlation matrix varies both locally and globally due to the changes in sub-pixel placement caused by geometric distortion. The above matrix appears to provide a good indication of the overall noise statistics of the image. Simulated images with the same small-scale noise correlations as the HDF drizzled images can be created by convolving an image which has independent noise in each pixel with the matrix shown in Table 4. The resulting image will have an RMS pixel noise identical to the input image, but because of the correlation introduced between neighboring pixels, the expected standard deviation of an $N \times N$ box of pixels (where N is much larger than 1) is $1/N$ times the sum of the above matrix elements, or about $1.9/N$. This procedure only simulates the correlation of pixels with equal intrinsic noise; a more complete simulation would need also to allow for the small pixel-to-pixel variations in the standard deviation of the noise.

5. The Images

Figure 8 shows a color composite of the HDF full field from the F450W, F606W, and F814W images. This image was produced from the initial version 1 data reduction, and has slightly lower S/N than the version 2 images. Nevertheless it reveals the striking variety of colors and morphologies of the distant galaxies visible in the field.

The final, combined images of the HDF which result from the drizzling process in each of the four filters are presented in Figs. 9 – 24. In each figure we display the co-added images from each of the four individual WFPC-2 CCD's. The total number of exposures and combined exposure time for each of the images is given in Table 5. Also shown are the sky levels, in units of data numbers (DN) per pixel (one DN corresponds to approximately 7 detected electrons). In the figures, the axes show pixel positions in the same units as the catalog listings. The scale at the bottom shows count levels in DN/1000 sec corresponding to different intensities on the final print. The images for the different bands have been scaled so that the maximum gray level corresponds to a constant AB magnitude of 20.35 magnitudes per square arcsec. The minimum gray level is set at -3 times the RMS of the sky level. For the dark gray levels in the images, therefore, a galaxy with a flat spectrum in f_ν will have a constant brightness in the different bands. However for fainter galaxies, the transfer functions diverge for the different bandpasses.

It is clear from visual inspection of the images that detection differ in each filter due the variations in their background noise levels. The higher background noise of the

F300W images, for which the individual exposures were all read-noise limited, is clearly evident. Objects that are present above the background noise display a wide variety of morphologies. At brightness levels well above the detection limit there are relatively few stars compared to the number of galaxies. The galaxies have a wide distribution of brightnesses, sizes, and shapes, and the brightest galaxies appear to correspond to the normal Hubble types. Most of the fainter sources also appear to be galaxies, although this must be established carefully because many of them are only marginally spatially resolved, but their morphologies are frequently chaotic and asymmetric. Not surprisingly, the fainter sources have a more compact appearance. To what extent this is an artifact of the $(1+z)^4$ diminution in surface brightness produced by increasing distance and the changing metric needs to be ascertained. Some of the fainter objects are undoubtedly bright H II regions and massive star complexes in galaxies, which appear above the background threshold while the remaining lower surface brightness regions of the galaxy do not. A cursory study of the images does not reveal any obvious heretofore unobserved class of objects compared to earlier HST images of moderately distant clusters such as 0939+4713 (Dressler et al. 1994b) and those associated with 3C 324 (Dickinson et al. 1996). There do appear to be a number of the linear structures having the sizes and luminosities of galaxies that have been noted by others (e.g. Cowie, Hu, & Songaila 1995). One of the most distinctive galaxies present in the field is a relatively large, extended, low-surface-brightness galaxy near the NW edge of WF3. This galaxy appears to be relatively nearby, and it might be an outlying galaxy member of one of the Ursa Major clusters. Color differences among the various galaxies are notable in that some of them appear much more prominent relative to neighboring galaxies in one of the filters than in others. Also, different colors in distinct regions of the same galaxy, such as the H II regions, are evident in many of the objects.

6. Source Detection and Photometry

6.1. Overview

The photometric parameters of very faint galaxies are difficult to measure and difficult to interpret in a straightforward way. Systematic errors can arise at every phase of the analysis. During the detection phase, spurious “galaxies” can be identified from noise peaks if the noise properties of the data are not well quantified; galaxies with unusual surface brightness profiles can be missed if their sizes are not well matched by the convolution kernel used to smooth the data. In the photometry phase, systematic errors can arise in converting from isophotal or aperture magnitudes to total magnitudes, in measuring colors based on isophotes defined in only one band, and in measuring moments or radii of

galaxies using only light from within a certain radius. In the source counting phase, galaxies may be overcounted if substructures are included as separate objects, or undercounted if overlapping distinct objects get counted as one source.

Such issues have generated considerable discussion in recent years. In constructing a catalog of objects which appear in the HDF, we have tried to take a fairly conservative approach, not digging deeply into the noise, and not adopting complex algorithms for source classification, weighted photometry, or merging and splitting of objects. As the data are public, we anticipate that others will generate their own catalogs. Indeed, comparisons among the various catalogs should be instructive in revealing the strengths and deficiencies of the various algorithms.

For the catalog we used a revised version of FOCAS (Jarvis & Tyson 1981; Valdes 1982). The program revisions are by Adelberger & Steidel (1996), and are intended to make the program more useful for HST and ground-based infrared imaging. A specific enhancement useful for our application is the ability to adjust isophotal detection thresholds as a function of position using variance maps. This is important for mosaiced data like the HDF, where the effective exposure time at the image boundaries is less than that at field center due to the telescope dithering process.

We shall limit our discussion here only to the version 2 catalog, which supercedes the initial catalog released with the HDF version 1 data. Source detection and deblending was carried out on the exposure-weighted sum of the F606W and F814W version 2 drizzled images to provide maximum limiting depth. The resulting catalog of objects is then applied to the registered images in each of the four individual bandpasses, so that photometry is carried out through identical apertures at all wavelengths. The F606W+F814W summed image is significantly deeper than any of the individual images, and few normal objects should be missed by using it to define the object catalog for all bands. It is possible, however, that objects with very strong emission lines in the F450W or F300W bands could have escaped detection.

To identify sources, the data are first convolved with a fixed smoothing kernel K_{ij} , shown in Table 6. Pixels with convolved values higher than a fixed threshold above a local sky background are marked as potentially being part of an object. A single value for σ_{sky} was measured for each CCD using a fit to the sky histogram, and then input as a parameter to the FOCAS catalog for object detection. FOCAS sets the detection threshold T to a constant times σ_{sky} :

$$T = N\sigma_{\text{sky}} \left(\sum_{i,j} K_{i,j}^2 \right)^{\frac{1}{2}}, \quad (5)$$

where the sum over the squares of the filter kernel elements accounts for the noise suppression *expected* for Poisson sky noise from the smoothing process. Note, however, that the pixel-to-pixel noise in the drizzled images is correlated (see §4.5), and therefore the *measured* pixel-to-pixel *rms* provides an underestimate of the “true” noise level of the image by a factor of 1.9. Smoothing the drizzled data does not suppress the noise as much as FOCAS expects for uncorrelated noise. We have therefore empirically adjusted the scaling factor N until the detection of spurious sources was minimized. In the end, a threshold $N = 4$ was adopted.

Note also that the sky *rms* is (relatively) larger on the PC than on the WFC detectors. Therefore the isophotal threshold in physical units (e.g. mag/square arcsecond) on the PC is somewhat higher than that used for the WFC.

After thresholding, regions consisting of more than a certain number of contiguous pixels (including diagonals) are counted as sources. For the HDF data, the source detection threshold was set to 4σ and the minimum area to 25 drizzled pixels, or 0.04 square arcseconds. This area is equivalent to 4 original WF pixels or 19.2 PC pixels. It corresponds to an isophotal diameter limit of roughly 0.2 arcsec, about 1.6 times larger than the FWHM of the PSF on the WF cameras. For a point source on the WFC, this minimum area encompasses roughly 60% of the total object flux. Correspondingly, isophotal fluxes of faint, extended galaxies with sizes close to the minimum size limit must underestimate their total fluxes by at least 40%.

These sources are then examined for sub-components using a variant of the original detection scheme. The detection filter is repeatedly run over the image as the threshold is raised. If, at some threshold, the object breaks into two or more unconnected regions, each fragment which meets the minimum area criterion of 25 pixels is given a separate sub-entry in the catalog, and the process continues.

One additional test was applied to potential “daughter” objects during the splitting process, using the FOCAS-defined “significance” parameter. This parameter is a measure of surface brightness difference between the object’s peak and its detection isophote, in units of the locally determined sky *rms* (see (Valdes 1982) for details). This “significance test” was not applied during the original detection of parent objects, as it largely duplicates the original isophotal thresholding criterion, but we have found empirically that its use helps to suppress the over-splitting of spurious sources from the extended wings of bright stars and large galaxies. Therefore a significance threshold of > 5 was imposed during object splitting.

The splitting process occasionally breaks large clumpy galaxies into many individual

sub-components, or produces many spurious sources along the diffraction spikes of bright stars. We have fixed the most egregious cases by manually merging the split objects back into their parent. The cases for which this was done are flagged with an “F” in the catalog below. In general, the only objects for which the splitting was adjusted manually were bright, unmistakably recognizable spiral galaxies, where FOCAS tends to sever off the arms and HII regions into separate objects. These have been re-merged back into the parent. There are many complex, irregular galaxies where we have allowed the original FOCAS splitting to stand, despite the fact that in some cases one’s intuition might suggest that the divided object is in fact a single entity. As noted below in §6.2, the catalog presented here includes *both parent and daughter objects*. The user may therefore adopt or reject the FOCAS splitting as he or she sees fit. In section 7 below, we present one possible algorithm for “re-merging” over-split objects, and apply it to the issue of galaxy number counts.

6.2. The Catalog

The source catalog is presented in Table 7. For each object we report the following parameters:

ID:

This is the FOCAS catalog entry number. The numbers after the decimal point indicate the level of splitting. Both parents and daughters are included in the catalog shown here. Thus many objects are included repeatedly in the catalog, both as part of the parent and as a separate daughter entry. For the statistical distributions shown in the next section, we have adopted specific color and separation criteria for merging objects to avoid double counting.

x,y:

The x and y pixel positions of each object, as defined by brightest pixel within the 3×3 pixel grid with the greatest luminosity within the detection area. For objects with a bright off-center peak, this position can be significantly different from the weighted center of the luminosity distribution within the detection area. For the HDF, such differences are typically less than 0.1 arcsec.

RA,DEC:

Minutes and seconds of the right ascension and declination corresponding to the x,y centers, epoch J2000. For RA these are minutes and seconds of time. To these must be added 12 hours (RA) and 62 degrees (Dec).

The RA and Dec positions given in Table 7 were derived as follows. The geometric distortion of each of the WFPC2 CCDs has been accurately measured (Trauger et al. 1995), and was removed in the drizzling stage of the image reduction process (see §4.5). The relative positions of the CCDs are somewhat less accurately determined, and indeed are known to drift with time. WFPC2 image headers are encoded with a world coordinate system tied to the HST guide star reference frame. Absolute positions in this reference frame may be incorrect by an arcsecond or more, depending on the position on the sky, and on the accuracy of the individual positions for the guide stars used during the HST observations.

We have recalibrated the absolute zeropoint of the HDF coordinates using interferometric radio positions for two sources within the HDF detected by both the Merlin array and the VLA. The radio astrometry for these was kindly provided by Tom Muxlow and Ken Kellerman, and the two independent radio measurements for each source agree with one another within their quoted uncertainties. Here, we have adopted the Merlin positions, whose positional accuracy is of ~ 20 mas or better. The WFPC2 coordinates for the optical counterparts of these two sources were compared to the Merlin positions, and a simple, mean translational offset ($\Delta\alpha = +0^s.089 \pm 0.010$ and $\Delta\delta = -1''.03$) was adopted and applied to the “raw” WFPC2 coordinates. A global solution using VLA sources detected in both the central field and the flanking fields (Windhorst 1996) yields a mean offset 0.4 arcseconds different from the one adopted above, but consistent to within uncertainties of the measured source coordinates.

The resulting coordinate system used for the HDF catalog should therefore be accurate (within the radio reference frame provided by the Merlin data) to approximately $0''.4$. Relative positions for individual galaxies are also typically accurate to $0''.1$, with the largest uncertainty coming from the ability of FOCAS to determine a peak position for faint, lumpy objects.

m_t, m_i:

The magnitudes of the detected sources in the F606W image. These magnitudes are in the AB system, where $m = -2.5 \log f_\nu - 48.60$. The “isophotal” magnitude m_i is determined from the sum of the counts within the detection isophote. The “total” magnitude is computed from the number of counts within a “grown” area. The total area is determined by first filling in any x or y concavities in the isophote shape and then adding by rings around the object until the area exceeds the detection area by at least a factor of two. For daughter objects, the total magnitude is divided between the daughters in proportion to their isophotal luminosities. The isophotal magnitudes correspond to the higher isophotes at which the object broke into multiple

components.

u – *b*, *b* – *v*, **and** *v* – *i*:

Colors within the detection area. These are essentially isophotal colors measured to a faint limiting isophote defined from the summed F606W+F814W image. They are expressed in the AB system. (Our preferred notation for these colors is $U_{300} - B_{450}$, $B_{450} - V_{606}$, and $V_{606} - I_{814}$, to avoid confusion with the groundbased Johnson and Strömrgren systems. However space in the tables does not allow us to use this convention here.) Galaxies where one band is a non-detection, as defined by having signal-to-noise ratio $S/N < 2$ within one of the bands, are marked as upper or lower limits (depending on which band drops out). If both bands are upper limits, no color is given.

S/N:

The signal-to-noise ratio of the detection in the summed F606W + F814W image, based on a semi-empirical noise model. If L_i is the sky-subtracted number of counts within the detection isophote, the expected variance is

$$(\Gamma\sigma(L_i))^2 = \Gamma N_{\text{obj}} + 1.9\sigma_{\text{sky}}^2 A_{\text{obj}} + A_{\text{obj}}^2 1.9\sigma_{\text{sky}}^2 / A_{\text{sky}}, \quad (6)$$

where Γ is the inverse gain (assumed to be 7 for all chips), N_{obj} is the total number of counts in the object aperture, A_{obj} and A_{sky} are the number of pixels within the object and sky apertures, respectively, and σ_{sky} is the measured standard deviation of the level within the sky aperture. The first term accounts for Poisson variations in total counts in the source aperture. The second term accounts for statistical variations in the mean sky level expected from Poisson statistics, and the third term accounts for the random (but not any systematic) uncertainty in determining the mean sky level within the sky aperture. The factor of 1.9 is an empirical correction to the measured pixel-to-pixel standard deviation to account for the fact that the images are in effect smoothed by the subsampling procedure. Therefore the pixel-to-pixel variance underestimates the variance that will be seen on large scales, as described above in §4.6. While this factor is in principle a function of scale, our detection apertures and sky apertures are large enough that a constant value is a good approximation.

A:

Area in pixels within the detection isophote.

r₁:

Intensity-weighted first-moment radius determined from pixels within the detection

isophote. The radii are determined relative to the x, y centers listed in the catalog, and the first moment radius is

$$r_1 = \sum rI(x, y) / \sum I(x, y), \quad (7)$$

where $I(x, y)$ is the intensity in each pixel.

PA:

The intensity-weighted position angle defined such that an object pointing North-South has $\theta = 0$, and the position angle increases as the major axis of the object rotates toward the east. In chip coordinates, the position angle is

$$\theta_{xy} = 0.5 \tan^{-1}[2Z/(Y - X)], \quad (8)$$

where X, Y , and Z are defined from the second moments of the image, as follows:

$$X = \sum x^2 I(x, y) / \sum I(x, y), \quad (9)$$

$$Y = \sum y^2 I(x, y) / \sum I(x, y), \text{ and} \quad (10)$$

$$Z = \sum xy I(x, y) / \sum I(x, y). \quad (11)$$

The nominal spacecraft roll (PA_V3) of 112° was assumed in converting from the measured position angle to a celestial position angle.

b/a :

The intensity-weighted axial ratio taken from the second moment of the light distribution. Define

$$P = X + Y, \text{ and} \quad (12)$$

$$Q = [(X - Y)^2 + 4Z^2]^{1/2}, \quad (13)$$

where X, Y , and Z are the moments defined above. Then the axial ratio is

$$\epsilon = [(P - Q)/(P + Q)]^{1/2}. \quad (14)$$

Flags: S indicates that the source is a single object (not split into subcomponents). B indicates that the outer isophote of the source overlaps a chip boundary in one or more bandpasses. F indicates that object components originally detected by FOCAS were manually merged back into their parent as described above.

7. Galaxy Counts

While it is not our purpose to discuss scientific results in this paper, it is useful to examine some of the basic statistics that will be important for such analyses.

The simplest statistic is the number of galaxies in the image. The counts of galaxies as a function of apparent magnitude are an essential tool of observational cosmology, and obtaining the faintest possible counts was one of the prime motivations behind the HDF project. However, before presenting the counts, it is useful to discuss the issue of object splitting, which has been a source of some interest for the faintest counts (Colley et al. 1996).

Figure 25 shows a section of the F606W image on chip 4, with the FOCAS identifications labeled. Examples of objects for which image splitting becomes problematical are sources 858, 774, and 555, which are actually among the most interesting sources in the entire HDF. Source 858 has been spectroscopically identified as a galaxy at $z = 3.226$ (Steidel et al. 1996). The spectrum refers to all four components, which have essentially the same color in the HDF image. Source 774 consists of three components which all have the same, very blue color. Source 555 consists of multiple components with different colors. The compact object 555.2 is very red and is probably a moderate-redshift elliptical galaxy. The elongated structure is spectroscopically identified as a galaxy at $z = 2.803$ (Steidel et al. 1996). FOCAS splits it into two objects 555.11 and 555.12. These subcomponents have nearly identical colors. In the catalog, we list the parents and all the daughters for these objects. *Many objects are therefore double-counted in the catalog.* In counting the galaxies, we must decide which components of the merged objects to keep separate, and which to count as a single object. The separations of the components of 858 and 747, for example, are under 100 kpc, even for an open cosmology. They are thus probably more fairly considered as pieces of a larger galaxy, rather than as separate entities. However, a simple separation criterion will often merge objects such as 555.1 and 555.2 that are likely to be chance projections rather than physical associations. We have therefore adopted criteria for merging daughters that combine both color and separation. Specifically, we require that $\Delta(V_{606} - I_{814}) < C$ and that the separation S_{ij} between two components be

$$S_{ij} < F \times (r_i + r_j), \quad (15)$$

where the radii are determined from the FOCAS isophotal area as $r_i = \sqrt{A/\pi}$ and the factor F is a tuneable parameter. The values $C = 0.3$ and $F = 5$ were chosen after some experimentation. These values merge all the components of sources 858 and 774, and merge the blue components of 555, leaving the red component as a separate object.

It is clearly a matter of subjective judgement whether to merge such objects. Does it

matter? Table 8 compares the counts in three magnitude intervals for our chosen values $F = 5, C = 0.3$; for values $F = 0, C = 0$, which provide maximal splitting (keeping only the daughters); and for $F = 100, C = 10$, which provide maximal merging (keeping only the parents). The change in counts from maximal to minimal merging is less than 20% in any magnitude interval. Thus splitting issues, while interesting and important for studies assessing the sizes, clustering, and morphology of faint galaxies, have only a small influence on the overall counts.

Incompleteness and uncertainties in the magnitude estimates also influence the counts. These are best addressed by means of simulations, and will be discussed in detail in Ferguson et al. (1996). For the purposes of this paper, it should be noted that FOCAS isophotal, total, and aperture magnitudes are each subject to certain systematic biases. The isophotal magnitudes, in particular, are likely to be approximately 0.2 mag fainter than total magnitudes for $V_{606} > 28$. The bias for total magnitudes is smaller but still non-negligible. The counts presented here have not been corrected for these biases. The counts are presented down to magnitudes at which they are likely to be more than 80% complete (under certain standard assumptions for the intrinsic surface-brightness distribution – see Ferguson et al. 1996 for details).

Figures 26 - 29 show the HDF counts in the individual bands. Isophotal, total, and aperture magnitudes are shown separately to illustrate the effects of different magnitude estimates. The counts in isophotal and total magnitudes are tabulated in Tables 9 and 10. Figure 30 shows the F450W and F814W band counts together with ground-based data. All the surveys have been corrected to AB magnitudes, but no color corrections have been applied.

The essential shape of the counts is relatively robust. In all bands the slopes flatten at faint magnitudes. The slopes in several magnitude intervals are given in Table 11 (computed from simple least-squares fitting of the binned data over the magnitude intervals shown). The rather sharp flattening in the F300W counts appears to be unlikely to be due to incompleteness (Ferguson et al. 1996), and quite possibly indicates that many of the galaxies at faint magnitudes have redshifts $z > 2$ such that they drop out of the F300W band due to the combined effects of internal extinction (which can be quite severe in the rest-frame far-UV), internal Lyman continuum absorption, and intergalactic absorption from the Lyman α forest and from Lyman-limit systems (Steidel et al. 1996; Madau et al. 1996). The flattening of the counts in the F450W band may signal the loss of galaxies at $z > 3$ due to the same effects.

Figures 31 – 33 show color–magnitude diagrams for galaxies in the field. For comparison, also shown are the colors for template non-evolving galaxies of different types.

The templates for E, Sbc, and Im galaxies are taken from Coleman, Wu, & Weedman (1980), with the extrapolations adopted by Ferguson & McGaugh (1995). We have normalized the E and Sbc spectra to have absolute magnitudes in the F450W band of $B_{450} = -21.1$, roughly L^* for $H_0 = 50 \text{ km s}^{-1} \text{ Mpc}^{-1}$. The Im spectrum is normalized to an absolute magnitude $B_{450} = -18$, more typical of a Magellanic irregular. The curves are labeled with redshift for galaxies of these assumed absolute magnitudes. It is interesting to note that while the elliptical galaxy template outlines the red envelope of the data reasonably well, there is a large population of galaxies at faint magnitudes that are bluer than the irregular galaxy template at any redshift. Also, as noted for the counts, there is a substantial number of galaxies with $U_{300} - B_{450}$ and $B_{450} - V_{606}$ colors and magnitudes consistent with being luminous ($\gtrsim L^*$) galaxies at high redshift ($z > 2$).

8. Conclusions

The Hubble Deep Field observations were taken with the expectation that they will contribute to the resolution of some of the outstanding questions in studies of galaxy formation. This paper describes the motivation, field and filter selection, and data reduction. Data, catalogs, and further information on the project are available on the World-Wide Web at <http://www.stsci.edu>.

We are extremely grateful to the large number of people who have contributed to the HDF project. In particular, we would like to acknowledge the efforts of the Advisory Committee, who donated a significant amount of effort in advising how best to use the Director's discretionary time, and in offering suggestions on how to carry out the observations. Among the many members of the STScI staff who helped with the observations, we would like to acknowledge especially J. C. Hsu and Ivo Busko for their timely efforts in developing software for data reduction. We thank Rogier Windhorst and Tom Muxlow for providing details on the comparison of radio and optical coordinates within the HDF.

Table 1. Characteristics of the Hubble Deep Field

Location:	12h 36m 49.4s +62°12'58" (Epoch J2000.0 / WFPC-2 'WFALL FIX' position) V3 Position angle = 112°
$E(B - V)$:	0.00
HI column density:	$1.7 \times 10^{20} \text{cm}^{-2}$
DIRBE flux:	$< 0.14 \text{MJy/ster}$
Radio sources:	none with flux $> 1 \text{ mJy}$ at 3.6 cm
IRAS cirrus:	Local minimum in $100\mu\text{m}$ maps
Bright stars:	None near the field
Galaxy Clusters:	Nearest is 48 armin away

Table 2. HDF Flanking Fields

Equatorial J2000 Coordinates	UT Date	N_{exp}	Total T_{exp} (s)	Comments
12 36 35.17 +62 13 38.7	30 Dec 1995	4	5300s	Inner West
12 36 20.93 +62 14 19.3	18 Dec 1995	3	2500s	Outer West
12 37 03.62 +62 12 17.2	30 Dec 1995	4	5300s	Inner East
12 37 17.83 +62 11 36.3	29 Dec 1995	3	3000s	Outer East
12 36 51.03 +62 15 47.6	30 Dec 1995	3	2500s	North West
12 37 05.27 +62 15 06.8	29 Dec 1995	3	2500s	North East
12 36 47.77 +62 10 08.4	29 Dec 1995	3	2500s	South East
12 36 33.56 +62 10 49.1	30 Dec 1995	3	2500s	South West

Table 3. Sky Noise Correlation Matrix

	$i - 1$	i	$i + 1$
$j - 1$	0.11	0.33	0.11
j	0.33	1.00	0.33
$j + 1$	0.11	0.33	0.11

Table 4. Noise Kernel

	$i - 1$	i	$i + 1$
$j - 1$	0.06	0.18	0.06
j	0.18	0.93	0.18
$j + 1$	0.06	0.18	0.06

Table 5. HDF Image Parameters

Filter	Number of Frames	Exposure Time (s)	10σ AB mag limit	Sky ^a PC1	Sky WF2	Sky WF3	Sky WF4
F300W	77	153700	26.98	39.259	78.642	92.954	89.686
F450W	58	120600	27.86	65.055	310.133	319.222	309.483
F606W	103	109050	28.21	238.507	1146.402	1155.758	1131.676
F814W	58	123600	27.60	158.615	768.667	771.862	754.104

^aSky values are total DN for the exposure times listed.

Table 6. FOCAS Smoothing Kernel

	$i - 2$	$i - 1$	i	$i + 1$	$i + 2$
$j - 2$	0	1	2	1	0
$j - 1$	1	3	3	3	1
j	2	3	4	3	2
$j + 1$	1	3	3	3	1
$j + 2$	0	1	2	1	0

Table 7. HDF Catalog

See attached pages.

Table 8. Counts for Various Amounts of Splitting

V_{606} range	$F = 5$ $C = 0.3$	$F = 0$ $C = 0$	$F = 100$ $C = 10$
23 – 25	137	128	133
25 – 27	491	528	450
27 – 29	1131	1239	1050

Table 9. HDF Galaxy Counts — F300W and F450W bands

AB mag	U_{300}			B_{450}		
	N	isophotal $\log(n)$ $\text{mag}^{-1} \text{deg}^{-2}$	total $\log(n)$ $\text{mag}^{-1} \text{deg}^{-2}$	N	isophotal $\log(n)$ $\text{mag}^{-1} \text{deg}^{-2}$	total $\log(n)$ $\text{mag}^{-1} \text{deg}^{-2}$
22.25	3	3.60	3.42	7	3.97	4.03
22.75	4	3.73	3.97	6	3.90	3.97
23.25	6	3.90	3.60	9	4.08	4.03
23.75	11	4.17	4.17	17	4.35	4.38
24.25	15	4.30	4.33	28	4.57	4.66
24.75	16	4.33	4.45	42	4.75	4.72
25.25	40	4.72	4.83	69	4.96	5.03
25.75	57	4.88	4.82	75	5.00	4.99
26.25	73	4.99	5.04	107	5.15	5.22
26.75	77	5.01	5.03	135	5.25	5.27
27.25	89	5.07	5.11	150	5.30	5.32
27.75	78	5.01	4.92	167	5.35	5.43
28.25	246	5.51	5.56
28.75	248	5.52	5.54
29.25

Table 10. HDF Galaxy Counts — F606W and F814W bands

		V_{606}		I_{814}		
AB mag	N	isophotal $\log(n)$ $\text{mag}^{-1} \text{deg}^{-2}$	total $\log(n)$ $\text{mag}^{-1} \text{deg}^{-2}$	N	isophotal $\log(n)$ $\text{mag}^{-1} \text{deg}^{-2}$	total $\log(n)$ $\text{mag}^{-1} \text{deg}^{-2}$
22.25	7	3.97	3.97	14	4.27	4.20
22.75	8	4.03	4.12	18	4.38	4.42
23.25	15	4.30	4.33	28	4.57	4.60
23.75	28	4.57	4.64	27	4.55	4.64
24.25	43	4.76	4.72	48	4.80	4.85
24.75	41	4.74	4.78	70	4.97	4.96
25.25	82	5.04	5.08	84	5.05	5.13
25.75	90	5.08	5.10	118	5.20	5.19
26.25	139	5.27	5.26	134	5.25	5.28
26.75	145	5.29	5.33	174	5.36	5.40
27.25	191	5.40	5.43	196	5.42	5.43
27.75	193	5.41	5.47	232	5.49	5.60
28.25	330	5.64	5.68	343	5.66	5.71
28.75	344	5.66	5.76	391	5.71	5.78
29.25	439	5.77	5.83

Table 11. Counts Slope

mag range	U_{300}	B_{450}	V_{606}	I_{814}
23 – 26	0.40	0.39	0.35	0.31
26 – 29	0.05 ^a	0.16	0.17	0.18

^aThe F300W limit here is 26-28; it is 26-29 for the other filters.

REFERENCES

- Adelberger, K., & Steidel, C. C. 1996, private communication
- Baggett, S., Casertano, S., & Biretta, J. 1995, Instrument Science Report WFPC2 95-07, (Baltimore: STScI)
- Bely, P., Petro, L., Elkin, D., & Kinney, E. 1996, in preparation
- Biretta, J. 1995, in *Calibrating Hubble Space Telescope: Post Servicing Mission*, ed. A. Koratkar & C. Leitherer (Baltimore: STScI), 257
- Biretta, J., Ritchie, C., & Rudloff, K. 1995, Instrument Science Report WFPC2 95-06, (Baltimore: STScI)
- Butcher, H., & Oemler, A. 1978, *ApJ*, 219, 18
- Butcher, H., & Oemler, A. 1984, *Nature*, 310, 31
- Coleman, G. D., Wu, C.-C., & Weedman, D. W. 1980, *ApJS*, 43, 393
- Colley, W. N., Rhoads, J. E., Ostriker, J. P., & Spergel, D. N. 1996, preprint
- Cowie, L. L., Hu, E. M., & Songaila, A. 1995, *AJ*, 110, 1576
- Dickinson, M. 1995a, in *Galaxies in the Young Universe*, ed. H. Hippelein, H.-J. Meisenheimer, & H.-J. Röser (Berlin: Springer), 144
- Dickinson, M. 1995b, in *Fresh Views on Elliptical Galaxies*, ASP Conf Series, ed. A. Buzzoni, A. Renzini, & A. Serrano (San Francisco: ASP), 283
- Dickinson, M., et al. 1996, in preparation
- Dressler, A., Oemler, A. J., Butcher, H. R., & Gunn, J. E. 1994a, *ApJ*, 430, 107
- Dressler, A., Oemler, A. J., Sparks, W. B., & Lucas, R. A. 1994b, *ApJ*, 435, L23
- Driver, S. P., Windhorst, R. A., & Griffiths, R. E. 1995, *ApJ*, 453, 48
- Driver, S. P., Windhorst, R. A., Ostrander, E. J., Keel, W. C., Griffiths, R. E., & Ratnatunga, K. U. 1995, *ApJ*, 449, L23
- Eisenhardt, P. 1995, private communication
- Ferguson, H. C., Dickinson, M. E., Giavalisco, M., Fruchter, A., Babul, A., & Katsanis, R. 1996, in preparation

- Ferguson, H. C., & McGaugh, S. S. 1995, *ApJ*, 440, 470
- Fruchter, A. S., & Hook, R. N. 1996, in preparation
- Giavalisco, M., Steidel, C. C., & Macchetto, D. 1996, *ApJ*, in press
- Glazebrook, K., Ellis, R., Colless, M., Broadhurst, T., Allington-Smith, J., & Tanvir, N. 1995, *MNRAS*, 273, 157
- Guhathakurta, P., Tyson, J. A., & Majewski, S. R. 1990, *ApJ*, 359, L9
- Jarvis, J. F., & Tyson, J. A. 1981, *AJ*, 86, 476
- Kellermann, K. 1995, private communication
- Leitherer, C. E. 1995, *HST Data Handbook*, version 2.0, (Baltimore: STScI)
- Lilly, S. J., Le Fevre, O., Crampton, D., Hammer, F., & Tresse, L. 1995, *ApJ*, 455, 50
- Madau, P. 1995, *ApJ*, 441, 18
- Madau, P., Ferguson, H. C., Dickinson, M., Giavalisco, M., Steidel, C. C., & Fruchter, A. S. 1996, submitted
- Oke, J. B. 1974, *ApJS*, 27, 21
- Petre, R. 1995, private communication
- Schade, D., Lilly, S. J., Crampton, D., Hammer, F., Le Fevre, O., & Tresse, L. 1995, *ApJ*, 451, L1
- Steidel, C. C., Giavalisco, M., Dickinson, M., & Adelberger, K. L. 1996, *AJ*, in press
- Steidel, C. C., & Hamilton, D. 1992, *AJ*, 104, 941
- Steidel, C. C., & Hamilton, D. 1993, *AJ*, 105, 2017
- Trauger, J. T., Vaughan, A. H., Evans, R. W., & Moody, D. C. 1995, in *Calibrating Hubble Space Telescope: Post Servicing Mission*, ed. A. Koratkar & C. Leitherer (Baltimore: STScI), 379
- Valdes, F. 1982, *Faint Object Classification and Analysis System* (KPNO Internal Publication)
- Windhorst, R. 1996, private communication

Yoshii, Y., & Peterson, B. 1994, ApJ, 436, 551

Fig. 1.— The HDF and flanking fields, superimposed on a ground-based 300 s *R*-band image taken with the Mayall 4-m telescope. The small labeled insets show centers of each flanking field image. The naming convention for the fields is given in the last column of table 2.

Fig. 2.— The bandpasses of the four filters chosen for the HDF. The total system throughput is shown, including the contribution from the filter, telescope and camera optics, and the detector.

Fig. 3.— Predicted background as a function of time for representative orbits (indicated as year.day) during early, middle, and late parts of the HDF observing period. The background model includes scattered light from the illuminated earth on the day side of the orbit, which causes the large modulation shown in the figure. The floor at 5×10^{-7} is from the zodiacal background and the excursion to zero is during earth-occultation.

Fig. 4.— HDF pointing positions. Nine dither positions were planned to cover the large scale (left panel) offsets simultaneously and to provide good sub-pixel sampling (right panel). The offsets are shown for the center of WF2 (after rotating x, y by 180 degrees to match WF4). The projection to WF (100 mas) sub-pixel locations varies significantly from chip to chip due to minor rotations and plate scale differences, as well as with position within a CCD due to differential geometric distortion. The symbols “*”, “o”, and “+” refer to the first, middle and last third of the exposure set for the F606W filter set plotted. A drift of about 10 mas occurred over multiple days. As noted in the text, dither positions 10 and 11 resulted from anomalous Fine Guidance Sensor tracking, and these frames also have a 4.3 arcminute rotation with respect to all the other data.

Fig. 5.— This figure illustrates the “footprint” of a pixel in the drizzling process. The dark region in the central pixel of this 3×3 grid shows the smaller area adopted for the pixel when it is projected onto the subsampled image.

Fig. 6.— This figure illustrates the major operations of drizzling. The location of each input pixel in the output subsampled image is determined from knowledge of the pointing position, rotation, and geometric distortion. The flux within that pixel is then “drizzled” into the overlapping output pixels in quantities proportional to the area of overlap.

Fig. 7.— The point-spread function of a bright star in the final drizzled HDF image.

Fig. 8.— A color composite image of the full HDF field, constructed from the F450W, F606W, and F814W images.

Fig. 9.— PC image in the F300W band. This and the following images are from the version 2 drizzled images. Exposure times are given in Table 5. The pixel scale at the borders is provided to allow galaxies in the catalog to be located via their x,y positions.

Fig. 10.— PC image in the F450W band.

Fig. 11.— PC image in the F606W band.

Fig. 12.— PC image in the F814W band.

Fig. 13.— WF2 image in the F300W band.

Fig. 14.— WF2 image in the F450W band.

Fig. 15.— WF2 image in the F606W band.

Fig. 16.— WF2 image in the F814W band.

Fig. 17.— WF3 image in the F300W band.

Fig. 18.— WF3 image in the F450W band.

Fig. 19.— WF3 image in the F606W band.

Fig. 20.— WF3 image in the F814W band.

Fig. 21.— WF4 image in the F300W band.

Fig. 22.— WF4 image in the F450W band.

Fig. 23.— WF4 image in the F606W band.

Fig. 24.— WF4 image in the F814W band.

Fig. 25.— A section of the F606W image from WF4, with the FOCAS identifications marked.

Fig. 26.— Galaxy counts as a function of AB magnitude in the F300W band. FOCAS total and isophotal magnitudes are shown for $22 < U_{300} < 28$. Aperture magnitudes are shown only for galaxies fainter than $U_{300} = 26$, because the brighter galaxies are almost all larger than the 0.5 arcsec radius aperture.

Fig. 27.— Galaxy counts as a function of AB magnitude in the F450W band. FOCAS total and isophotal magnitudes are shown for $22 < B_{450} < 29$. Aperture magnitudes are shown only for galaxies fainter than $B_{450} = 26$.

Fig. 28.— Galaxy counts as a function of AB magnitude in the F606W band. FOCAS total and isophotal magnitudes are shown for $22 < V_{606} < 29.5$. Aperture magnitudes are shown only for galaxies fainter than $V_{606} = 26$.

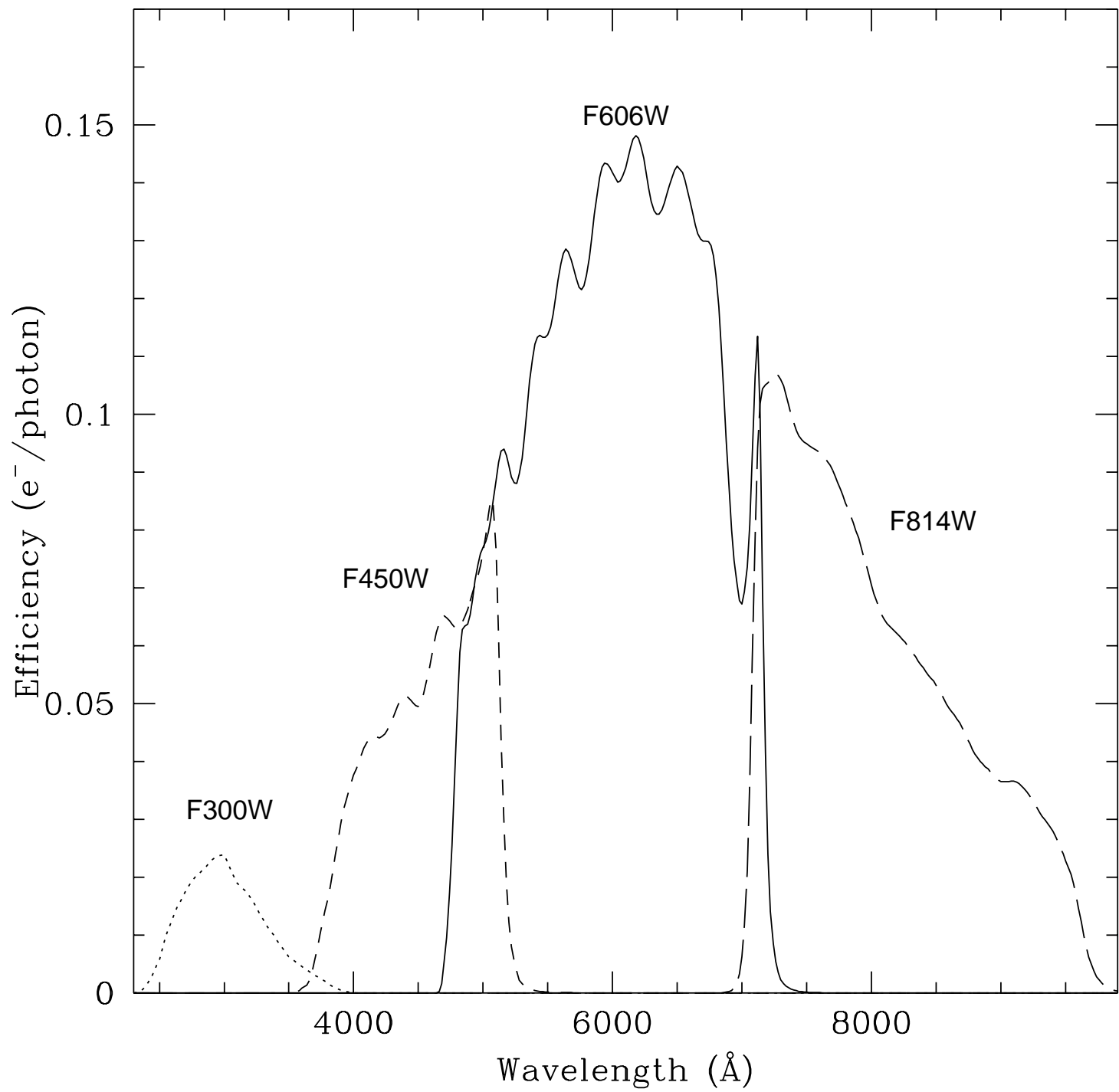
Fig. 29.— Galaxy counts as a function of AB magnitude in the F814W band. FOCAS total and isophotal magnitudes are shown for $22 < I_{814} < 29$. Aperture magnitudes are shown only for galaxies fainter than $I_{814} = 26$.

Fig. 30.— Galaxy counts as a function of AB magnitude in the F450W and F814W bands, together with a compilation of existing ground-based data. FOCAS total and isophotal magnitudes are shown for $22 < I_{814} < 29$. No color corrections have been applied to the ground-based data.

Fig. 31.— Color-magnitude diagram $U_{300} - B_{450}$. Galaxies detected at more than 5σ are shown as large hexagons. Galaxies detected at less than 5σ are smaller hexagons. Galaxies either undetected in F300W or detected at less than 2σ significance are shown as open triangles at the position of the 2σ limit on the color. Also shown are the colors of fiducial non-evolving spectra of E, Sbc, and Im galaxies (see text), as dotted, solid, and dashed curves, respectively.

Fig. 32.— Color-magnitude diagram $B_{450} - V_{606}$. The meanings of the lines and symbols are the same as for the previous figure. Triangles are shown at the position of the F450W 2σ limits.

Fig. 33.— Color-magnitude diagram $V_{606} - I_{814}$. The meanings of the lines and symbols are the same as for the previous two figures. Triangles are shown at the position of the F606W 2σ limits.



Examples of F606W Orbital Background

